Nano Research Energy

ISSN 2791-0091 (print); 2790-8119 (online)
https://doi.org/10.26599/NRE.2026.9120232

Research Article

Asymmetric Fe-N_4-O sites enabled by axial oxygen coordination for high-efficiency Zn-air batteries

Wei Liu[1], Yu Liang[1], Mengtian Huo[1], Jie Xi[1], Xiaowen Gu[1], Nan Ma[1], Maoyu Wang[3], Zihao Xing[1,2] (✉), and Jinfa Chang[1,2] (✉)

[1] *Key Laboratory of Polyoxometalate and Reticular Material Chemistry of Ministry of Education, Faculty of Chemistry, Northeast Normal University, Changchun* 130024, *China*
[2] *Key Laboratory of Advanced Energy Materials Chemistry* (*Ministry of Education*), *Nankai University, Tianjin* 300071, *China*
[3] *Shanghai Synchrotron Radiation Facility, Shanghai Advanced Research Institute, Chinese Academy of Sciences, Shanghai* 201204, *China*

Received: 22 January 2026 / **Revised:** 27 March 2026 / **Accepted:** 7 April 2026 / **Published date:** 9 May 2026

ABSTRACT

Iron-nitrogen-carbon (Fe-N-C) catalysts are a promising class of non-precious electrocatalysts for the oxygen reduction reaction (ORR), with strong potential for integration into emerging energy technologies. Here, an oxygen-bridged axial coordination strategy is employed to anchor iron phthalocyanine (FePc) onto manganese oxide decorated carbon nanotubes (Mn_3O_4-CNTs). The resulting synergy between asymmetric Fe-N_4-O sites and heterojunction interfaces finely tailors the local coordination of Fe centers, which induces electron transfer from the Fe center to the axial O atom and downshifts the Fe d-band center, thereby weakening the adsorption strength of oxygen-containing intermediates and substantially boosting ORR activity. In alkaline media, the optimized FePc-Mn_3O_4-CNTs catalyst exhibits a high half-wave potential ($E_{1/2}$) of 0.89 V vs. reversible hydrogen electrode (RHE), a low Tafel slope of 41.51 mV·dec^{-1}, and follows an efficient four-electron pathway. This catalytic performance translates directly into a zinc-air battery that delivers a peak power density of 171.81 mW·cm^{-2}, a specific capacity of 754.12 mAh·g^{-1}, and stable operation for 160 h. This work demonstrates a coordinated strategy combining axial coordination engineering with heterojunction design to synergistically optimize the catalytic properties of Fe-N-C molecular catalysts.

KEYWORDS

axial oxygen coordination, heterojunction effect, Fe-N_4-O active sites, asymmetric single-atom sites

1 Instruction

Improving the efficiency of advanced electrochemical energy-conversion systems fundamentally rely on reducing irreversible energy losses at the cathode, where the sluggish oxygen reduction reaction (ORR) imposes a persistent kinetic limitation [1–5]. The challenge lies in cleaving the stable O=O bond while managing complex multi-electron transfer steps, which together constitute a major efficiency bottleneck [6, 7]. Although platinum-based catalysts show superior activity, their high cost and scarcity hinder widespread adoption [8–11]. This urgent need has driven extensive research into economical and robust non-precious-metal catalysts [12]. Among them, iron-nitrogen-carbon (Fe-N-C) structures have gained attention for their tunable electronic configurations and catalytic promise [13, 14]. However, conventional preparation methods, especially high-temperature pyrolysis, often yield catalysts with ill-defined active sites, where iron aggregation and inconsistent coordination environments are common [15–17]. Such structural ambiguity obscures the relationship between geometry and catalytic function, leading to limited reaction efficiency and inadequate long-term stability [1]. Overcoming these limitations requires advanced fabrication strategies that enable precise control over the local atomic architecture and electron density at catalytic sites, along with strong interaction with the underlying support. Integrating tailored coordination design, electronic fine-tuning, and reinforced interfacial interaction offers a synergistic route to fully realize the potential of Fe-N-C catalysts for practical, durable applications [18, 19].

Iron phthalocyanine (FePc) is widely regarded as a model Fe-N_4 catalyst among non-precious metal systems, owing to its well-defined molecular structure, which provides an ideal atomic-scale platform for studying how coordination geometry influences electrocatalytic activity [20–22]. Current strategies to enhance FePc performance generally follow three main directions. The first is planar engineering, in which FePc molecules are supported on conductive carbon materials to improve charge transfer [23]. However, this approach largely preserves the planar D_{4h}-

© The Author(s) 2026. Published by Tsinghua University Press. The articles published in this open access journal are distributed under the terms of the Creative Commons Attribution 4.0 International License (http://creativecommons.org/licenses/by/4.0/), which permits use, distribution and reproduction in any medium, provided the original work is properly cited.

Address correspondence to Zihao Xing, xingzh612@nenu.edu.cn; Jinfa Chang, changjinfa@nenu.edu.cn

symmetric structure of FePc, offering limited ability to tun the local chemical environment of the iron center [24]. The second is curvature engineering, where the planar geometry of the phthalocyanine molecule is modified through molecular design or strain to induce deviations from planarity, thereby regulating its electronic structure [25, 26]. Nonetheless, this method can compromise molecular stability and often lacks the controllability needed for uniform deformation, adversely affecting reproducibility and durability. The third strategy is axial engineering, which involves attaching axial ligands to the iron center for direct electronic tuning [6, 27, 28]. However, this approach is largely confined to carbon-based supports and exhibits limited interfacial synergy [29]. Although these strategies have led to some performance improvements, they remain insufficient in simultaneously addressing the multiple challenges of enhancing intrinsic activity, improving structural stability, and facilitating efficient charge transfer. Thus, designing novel composite strategies that concurrently tailor the electronic structure of FePc and the interfacial properties of the support has emerged as a crucial pathway for advancing FePc-based electrocatalysts [30].

Building on this background, we propose a novel oxygen-bridged axial coordination strategy to create Fe-N_4-O linkages between FePc units and manganese oxide decorated carbon nanotubes (Mn_3O_4-CNTs). This approach yields a composite catalyst in which the Mn_3O_4-CNTs support not only provides a stable coordination interface and conductive network but also enhances charge transfer and stability through heterojunction effects. The resulting catalyst exhibits excellent alkaline ORR performance, including a half-wave potential of 0.89 V vs. reversible hydrogen electrode (RHE), a Tafel slope of 41.51 mV·dec^{-1}, and a dominant four-electron pathway. When applied in a zinc-air battery, it delivers an open-circuit voltage of 1.50 V, a peak power density of 171.81 mW·cm^{-2}, and a specific capacity of 754.12 mAh·g^{-1}. Overall, this work presents an innovative route to design efficient Fe-N-C electrocatalysts by integrating axial coordination design with heterojunction interface engineering, offering a new paradigm for constructing high-performance molecular frameworks for oxygen reduction and related applications.

2 Experimental

2.1 Materials and synthesis

2.1.1 Chemicals

Multi-walled CNTs were purchased from Tanfeng Tech. Inc. Iron (II) Phthalocyanine (FePc, 98%), N, N-Dimethylformamide (DMF, AR), $Mn(OAC)_2{\cdot}4H_2O$, $Zn(OAC)_2{\cdot}2H_2O$, RuO_2 and Pt/C (20 wt.%) were obtained from Aladdin Reagent. KOH was sourced from Tianjin Xinbote Chemical Co., LTD. Ammonia solution ($NH_3{\cdot}H_2O$, 25%) was obtained from Tianjin Beichen Fangzheng Reagent Factory. All chemical were of analytical grade and used without further purification.

2.1.2 Synthesis of Mn_3O_4-CNTs

First, carbon nanotubes (CNTs, 200 mg) were activated by heating at 500 °C for 3 h. Subsequently, $Mn(OAC)_2{\cdot}4H_2O$ (0.8 mmol) was mixed with deionized water (8 mL) and ultrasonicated for 10 min to obtain a clear and homogeneous solution. Ammonia solution ($NH_3{\cdot}H_2O$) was added dropwise under stirring (1200 rpm) until the pH reached 11, followed by continued stirring for 30 min. An ethanol-water mixture (8 mL, V_{EtOH}/V_{H_2O} = 1/1) and the pre-treated CNTs were then introduced. The mixture was stirred at 60 °C and 1200 rpm for 12 h. The resulting suspension was transferred to a 50 mL Teflon-lined autoclave and heated at 150 °C for 3 h. The product was collected by centrifugation (6000 rpm), washed three times with an ethanol-water solution mixture (V_{EtOH}/V_{H_2O} = 1/1), and freeze-dried to obtain Mn_3O_4-CNTs.

2.1.3 Synthesis of FePc-Mn_3O_4-CNTs and FePc-CNTs

In a typical procedure, FePc (6 mg) and Mn_3O_4-CNTs (30 mg) were separately dispersed in 10 and 30 mL of DMF by sonication for 100 min to form uniformly dispersed suspensions. The FePc dispersion was then added dropwise to the Mn_3O_4-CNTs suspension. The mixture was sonicated for another 1 h and then stirred at ambient conditions for 24 h. The resulting slurry was centrifuged, washed alternately six times with deionized water and anhydrous ethanol, and finally vacuum freeze-dried to obtain FePc-Mn_3O_4-CNTs. FePc-CNTs were prepared similarly, using CNTs instead of Mn_3O_4-CNTs.

3 Results and discussion

The synthetic pathway for the FePc-Mn_3O_4-CNTs heterostructured catalyst, based on molecular self-assembly, is illustrated in Fig. 1(b). Initially, Mn_3O_4 nanoparticles were grown *in-situ* on carbon nanotubes (CNTs) via a hydrothermal method, yielding the Mn_3O_4-CNTs composite support [31, 32]. Subsequently, through a self-assembly process driven by chemical bonding, FePc molecules were firmly anchored onto the Mn_3O_4 surface, producing the FePc-Mn_3O_4-CNTs composite catalyst with strong interfacial interactions. For reference, FePc-CNTs were fabricated using the same assembly route without Mn_3O_4.

Microscopic morphology and nanostructure of the synthesized catalysts were examined by scanning and transmission electron microscopy (SEM/TEM). SEM and TEM images confirm the successful decoration of Mn_3O_4 nanoparticles on the CNTs (Figs. S1–S6 in the Electronic Supplementary Material (ESM)). FePc-Mn_3O_4-CNTs largely retain the bulk Mn_3O_4 nanoparticle morphology of the Mn_3O_4-CNTs support (Fig. 1(b)). High-resolution TEM (HRTEM) was employed to further verify the anchoring state of FePc on Mn_3O_4-CNTs. Analysis of lattice fringes reveals an interlayer spacing of 0.492 nm, corresponding to the (101) plane of Mn_3O_4, consistent with the selected-area electron diffraction (SAED) pattern in Fig. 1(d). The SAED pattern also shows lattice spacings of 0.492 and 0.288 nm for the (101) and (200) planes of Mn_3O_4 in FePc-Mn_3O_4-CNTs, aligning with those of pure Mn_3O_4-CNTs (Fig. 1(c), Fig. S7 in the ESM) [33]. This indicates that the crystal structure of Mn_3O_4 is preserved after FePc loading. High-angle annular dark-field scanning transmission electron microscopy (HAADF-STEM) images show that FePc-Mn_3O_4-CNTs particles are approximately 100 nm in size (Fig. 1(f)). Corresponding energy-dispersive X-ray spectroscopy (EDS) elemental mapping confirms the uniform distribution of C, N, O, Mn, and Fe, with Fe primarily localized within the Mn_3O_4 regions (Figs. 1(g)–1(k)). STEM line-scan EDS further validates the elemental distribution and indicates that the Fe content is lower than that of Mn (Fig. 1(e)), in agreement with ICP-OES results (Table S1 in the ESM). Importantly, magnified images clearly reveal FePc forming a thin coating on the Mn_3O_4 nanoparticle surfaces (Fig. 1(l)).

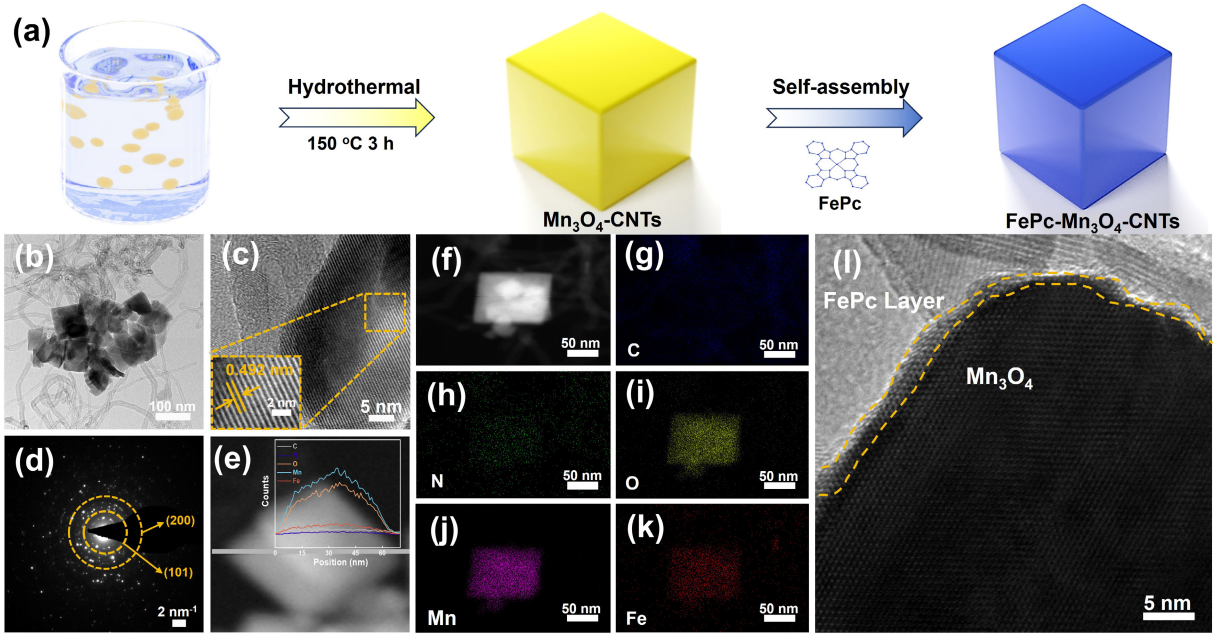

Figure 1 (a) Scheme of the synthetic procedure for FePc-Mn_3O_4-CNTs. (b) TEM and (c) High-resolution TEM images of FePc-Mn_3O_4-CNTs. (d) SAED image of FePc-Mn_3O_4-CNTs. (e)The STEM-EDS line-scan profiling for FePc-Mn_3O_4-CNTs. (f-k) HAADF-STEM and corresponding EDS elemental maps of FePc-Mn_3O_4-CNTs. (l) HAADF-STEM image of FePc-Mn_3O_4-CNTs.

X-ray diffraction (XRD) patterns exhibit distinct diffraction peaks assignable to Mn_3O_4 (PDF#18-0803) and crystalline FePc in FePc-Mn_3O_4-CNTs, confirming the successful immobilization of FePc on Mn_3O_4 while preserving its structure (Fig. 2(a)) [34]. Raman spectra of FePc-Mn_3O_4-CNTs show a distinct Mn-O vibrational band at 656 cm^{-1} attributed to Mn_3O_4, while spectral features corresponding to the macrocyclic framework of FePc remain observable in the 600–800 cm^{-1} range (Fig. S8(a) in the ESM) [35, 36]. Fourier transform infrared (FTIR) spectroscopy detects characteristic vibrational signatures from both Mn_3O_4 and FePc in FePc-Mn_3O_4-CNTs. Specifically, Mn_3O_4 exhibits peaks at 520 and 626 cm^{-1}, corresponding to Mn-O vibrations from octahedral and tetrahedral sites, respectively (Fig. S8(b) in the ESM) [37]. Additionally, FePc shows characteristic absorption: an out-of-plane C-H deformation at 726 cm^{-1}, metallophthalocyanine ring skeletal vibrations at 1117 and 1330 cm^{-1}, C-N stretching near 1162 cm^{-1}, aromatic ring vibrations around 1418 cm^{-1}, and an Fe-N signal at 893 cm^{-1} [21, 24]. These results collectively confirm that the molecular structure of FePc remains intact after loading. Notably, electron paramagnetic resonance (EPR) spectroscopy reveals a paramagnetic signal near g = 2.003 for Mn_3O_4-CNTs, attributed to electrons trapped by oxygen vacancies, confirming abundant oxygen vacancies (Fig. S9 in the ESM) [38, 39]. In summary, the above characterizations verify that FePc is successfully anchored on the Mn_3O_4 surface while maintaining its intact molecular structure.

To investigate differences in chemical states and electronic coordination environments between the heterostructured FePc-Mn_3O_4-CNTs and FePc-CNTs, X-ray photoelectron spectroscopy (XPS) and X-ray absorption spectroscopy (XAS) were performed. XPS survey spectra confirm the presence of C, N, O, Mn, and Fe in FePc-Mn_3O_4-CNTs, verifying successful loading of FePc onto the Mn_3O_4-CNTs support (Fig. S10 in the ESM). The Fe 2p spectra of FePc-Mn_3O_4-CNTs display signatures of Fe^{2+} and Fe^{3+} species, with Fe $2p_{3/2}$ peaks at 709.3 and 712.0 eV and corresponding Fe $2p_{1/2}$ peaks at 721.9 and 724.8 eV, each accompanied by satellite structures. Compared with FePc-CNTs, the Fe $2p_{3/2}$ peaks in FePc-Mn_3O_4-CNTs show a positive shift of approximately 0.4 eV (Fig. 2(b)) [6, 40, 41]. The N 1s spectral of FePc-Mn_3O_4-CNTs exhibits peaks at 399.1 and 400.6 eV, attributed to Fe-coordinated N and pyridinic N, respectively. The binding energy of the Fe-N peak increases by 0.2 eV relative to FePc-CNTs (Fig. S11(a) in the ESM) [31, 42, 43], indicating reduced electron density around both Fe and N atoms. Conversely, the Mn 2p spectra of FePc-Mn_3O_4-CNTs show a different trend. Signals corresponding to Mn^{2+}, Mn^{3+}, and Mn^{4+} species appear in the Mn $2p_{3/2}$ region at 640.8, 642.3, and 644.5 eV, respectively, with their Mn $2p_{1/2}$ counterparts at 651.8, 653.4, and 655.0 eV (Fig. 2(c)) [44]. These peaks exhibit a uniform negative shift of 0.2 eV relative to pristine Mn_3O_4-CNTs. Similarly, in the O 1s spectrum of FePc-Mn_3O_4-CNTs peaks corresponding to Mn-O-Mn, oxygen vacancies (O_v), hydroxyl groups (OH), and carbonyl groups (C=O) shifted downward by 0.4 eV compared with Mn_3O_4-CNTs (Fig. S11(b) in the ESM) [45]. This series of binding energy changes confirms that the heterojunction between FePc and Mn_3O_4-CNTs induces interfacial electron rearrangement. UPS results provide further evidence for this interfacial interaction. The work function (Φ) of Mn_3O_4-CNTs is calculated as 4.14 eV, higher than that of FePc-CNTs (3.93 eV) (Figs. S12(a)-S12(i)), S13 in the ESM, Figs. 2(c) and 2(d)). This differential facilitates electron transfer from the material with lower work function (FePc) to that with higher work function (Mn_3O_4-CNTs). Thus, combined XPS and UPS evidence confirms electron migration from the FePc component to the Mn_3O_4-CNTs support [46].

The local coordination geometry and electronic structure of the FePc-Mn_3O_4-CNTs heterojunction were probed using X-ray absorption near-edge structure (XANES) and extended X-ray absorption fine structure (EXAFS) analyses. The Fe K-edge XANES data showed that the absorption edge energy for FePc-Mn_3O_4-CNTs lies between those of Fe foil and FePc, closer to FePc, indicating an average Fe oxidation state near +2 (Fig. 2(e)). A noticeable shift of the absorption edge to higher energies relative to FePc-CNTs reflects an altered electronic structure and increased valence state of Fe, consistent with electron migration from FePc

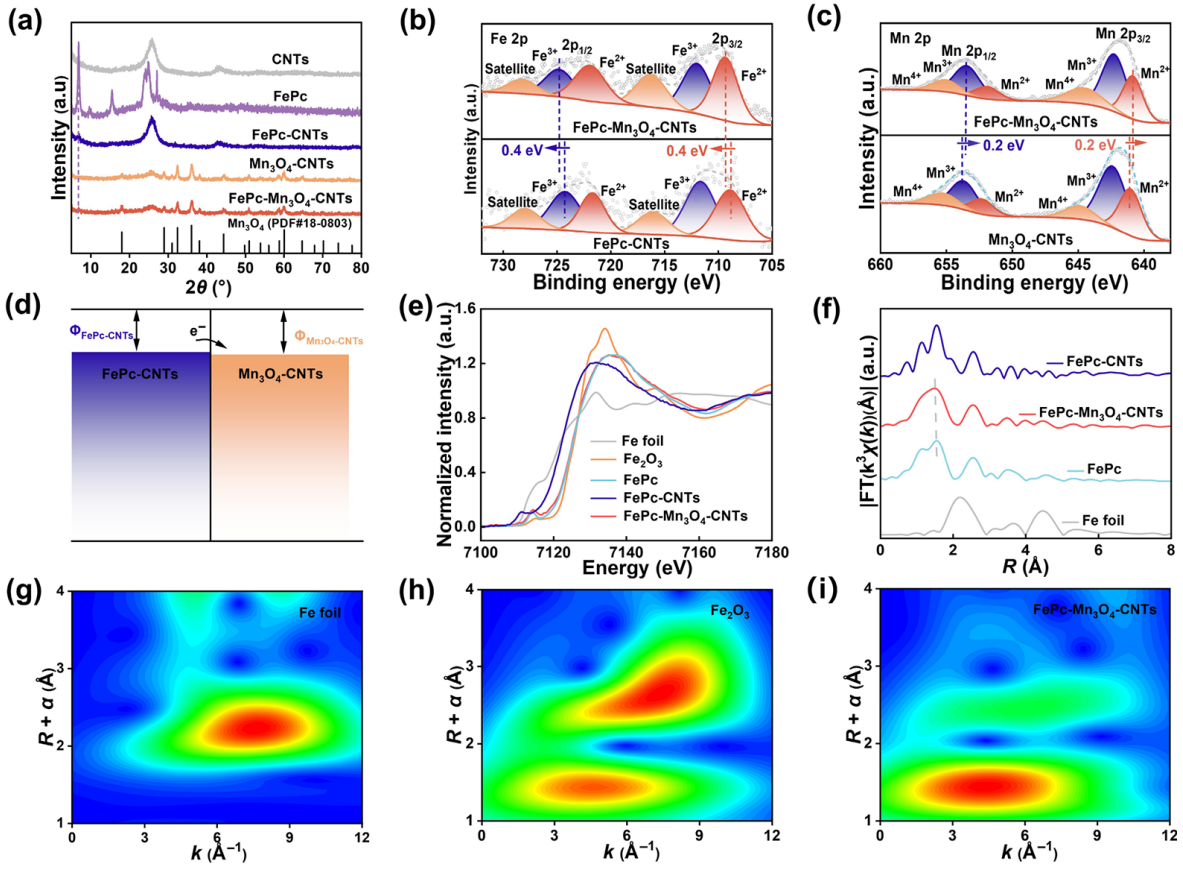

Figure 2 (a) XRD patterns of the synthesized samples. (b) Fe 2p XPS spectra for FePc-Mn_3O_4-CNTs and FePc-CNTs. (c) Mn 2p XPS spectra for FePc-Mn_3O_4-CNTs and Mn_3O_4-CNTs. (d) Schematic illustration of the electronic interfacial interaction between FePc-CNTs and Mn_3O_4-CNTs. (e) Normalized Fe K-edge XANES spectra for FePc-Mn_3O_4-CNTs, FePc-CNTs, FePc, Fe_2O_3 and Fe foil. (f) FT-EXAFS spectra at the Fe K-edge for FePc-Mn_3O_4-CNTs, FePc-CNTs, FePc, and Fe foil. (g–i) WT plots for Fe foil, Fe_2O_3, and FePc-Mn_3O_4-CNTs.

to Mn_3O_4-CNTs as indicated by XPS. In the pre-edge region (Fig. S14 in the ESM), a weak additional peak appears at 7117.3 eV for FePc-Mn_3O_4-CNTs compared to ideal FePc-CNTs. This feature corresponds to the normally forbidden 1s to 3d quadrupole transition of the Fe center under square-planar symmetry (D_{4h}) [32]. Its emergence signifies a reduction in local symmetry from D_{4h} to C_{4v} at the Fe-N_4 site due to axial bonding with oxygen-based ligands, resulting in an asymmetric Fe-N_4-O active configuration that fine-tunes the electronic arrangement at the iron center. In the Fourier-transformed EXAFS (FT-EXAFS) spectrum (Fig. 2(f)), a prominent signal near 1.49 Å is assigned to Fe-N/O coordination paths. The absence of a discernible Fe-Fe coordination signal further confirms the monatomic distribution of iron species [31]. EXAFS fitting yields structural parameters consistent with an Fe-N_4-O coordination configuration in FePc-Mn_3O_4-CNTs (Figs. S15(a), S15(b), S16, Table S2 in the ESM). Wavelet transform (WT) analysis of the Fe K-edge EXAFS data provides additional verification, showing a distinct intensity maximum at 4.32 $Å^{-1}$ corresponding to Fe-N/O bonding (Figs. 2(g)–2(i), Fig. S17 in the ESM). This result confirms specific coordination of Fe with N and O, with no evidence of metal-cluster formation. In summary, these findings demonstrate that the Fe center in FePc-Mn_3O_4-CNTs adopts an Fe-N_4O coordination structure, with local symmetry transformed from square-planar to axially coordinated lower symmetry, accompanied by significant charge transfer from FePc to Mn_3O_4-CNTs. This precise coordination tuning offers crucial local structural insights into the enhanced electrocatalytic performance.

To evaluate the ORR performance differences arising from asymmetric Fe-N_4-O versus symmetric Fe-N_4 coordination environments, FePc-Mn_3O_4-CNTs were tested in O_2-saturated 0.1 M KOH electrolyte. Cyclic voltametric (CV) profiles recorded from 0 to 1.0 V vs. RHE show that FePc-Mn_3O_4-CNTs exhibits a markedly enhanced reduction signal compared with FePc-CNTs, directly demonstrating that Fe-O coordination substantially boosts the activity of its active centers (Figs. S18(a)–S18(c) in the ESM). Linear sweep voltammetry (LSV) measurements reveal that FePc-Mn_3O_4-CNTs achieves an onset potential of 0.97 V and a half-wave potential ($E_{1/2}$) of 0.89 V vs. RHE, outperforming both FePc-CNTs, Fe-N-C and Pt/C (Figs. 3(a)–3(c), Figs. S19–S22 in the ESM). Its $E_{1/2}$ also surpasses those of previously reported FePc-based catalysts prepared under similar conditions (Tables S3 and S4 in the ESM). With a Tafel slope of 41.51 $mV·dec^{-1}$, FePc-Mn_3O_4-CNTs demonstrates superior kinetics compared to FePc-CNTs (56.48 $mV·dec^{-1}$) and Pt/C (96.28 $mV·dec^{-1}$) (Fig. 3(d)). Consistently, the kinetic current density (J_k) and mass activity of FePc-Mn_3O_4-CNTs are significantly higher, reaching 53.26 $A·g^{-1}$ at 0.85 V vs. RHE (Fig. 3(e)).

Electrochemical impedance spectroscopy (EIS) reveals that FePc-Mn_3O_4-CNTs exhibits lower charge-transfer resistance than FePc-CNTs and Mn_3O_4-CNTs, indicating that the newly formed Fe-O-Mn bond effectively promotes electron transfer (Fig. 3(f)). Across the potential range of 0.2–0.8 V vs. RHE, FePc-Mn_3O_4-CNTs achieves an electron-transfer number (n) close to 3.96, with a hydrogen-peroxide yield below 5% (Fig. 3(g)), indicating a highly efficient $4e^-$ transfer pathway and high selectivity. The

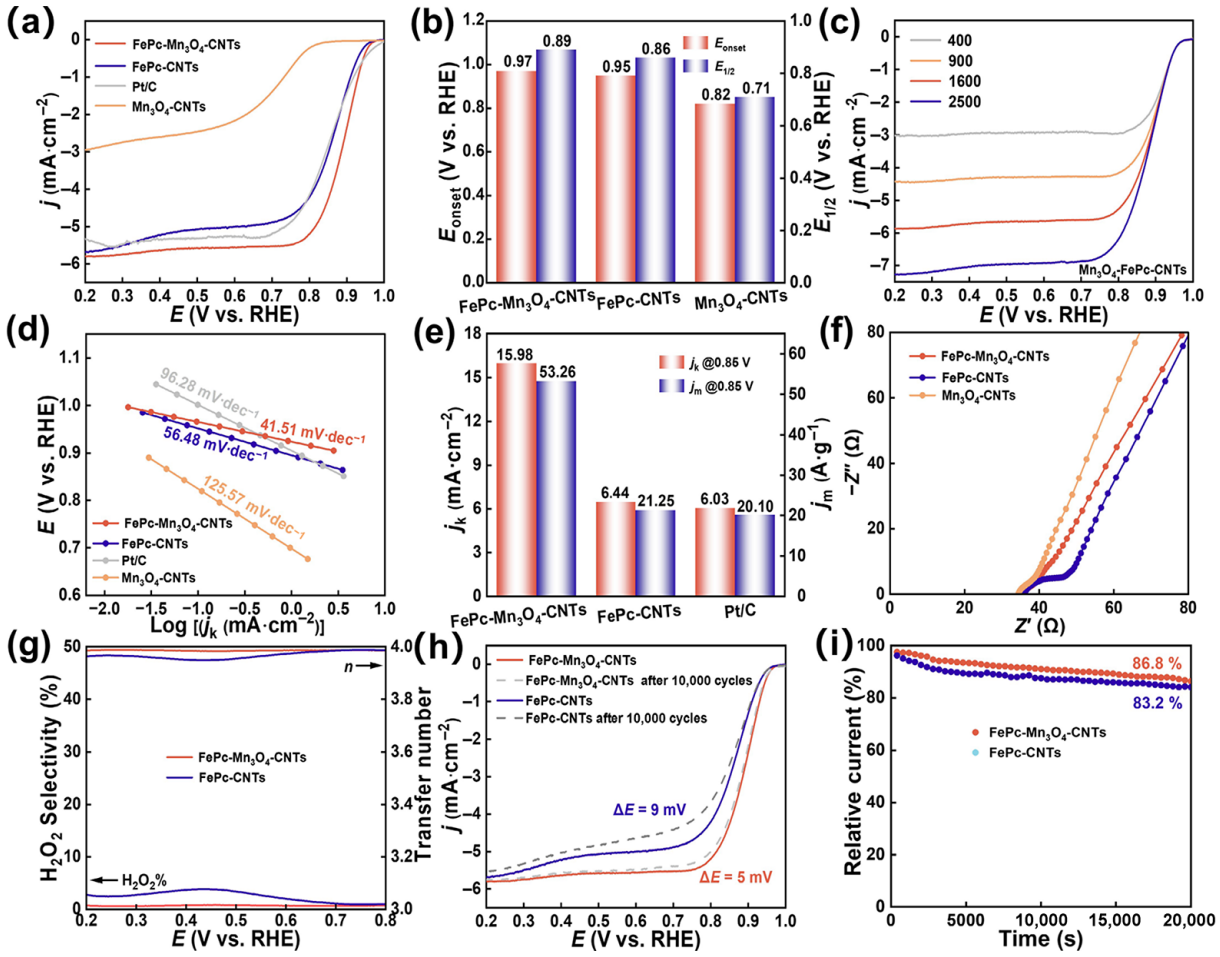

Figure 3 (a) LSV curves of various catalysts. (b) Onset potential (E_{onset}) and half-wave potential ($E_{1/2}$) of various catalysts. (c) LSV curves of FePc-Mn_3O_4-CNTs at different *r.p.m.* (d) Tafel plots of various catalysts. (e) Kinetic current density (J_k) and mass activity (J_m) at 0.85 V vs. RHE for various catalysts. (f) Nyquist plots from EIS measurements for various catalysts. (g) H_2O_2 yield and electron transfer numbers (n) for FePc-Mn_3O_4-CNTs and Mn_3O_4-CNTs. (h) LSV curves of FePc-Mn_3O_4-CNTs and FePc-CNTs before and after 10,000 cycles. (i) Chronoamperometric (i–t) stability tests for the iron-based samples.

double-layer capacitance (C_{dl}) of FePc-Mn_3O_4-CNTs is 13.46 mF·cm^{-2}, higher than those of 11.55 mF·cm^{-2} for FePc-CNTs and 2.56 mF·cm^{-2} for Mn_3O_4-CNTs (Figs. S23(a)–S23(f) in the ESM), suggesting an expanded electrochemical interface with more accessible active sites. Regarding stability, after 10,000 accelerated durability test cycles, FePc-Mn_3O_4-CNTs shows only a 5 mV negative shift in $E_{1/2}$, outperforming the 9 mV decay of FePc-CNTs (Fig. 3(h)). Amperometric i–t testing further confirms its stability, with FePc-Mn_3O_4-CNTs retaining 86.8% of its initial current after 20,000 s continuous operation, compared to a 16.8% decay for FePc-CNTs (Fig. 3(i)).

The post-reaction XRD patterns of FePc-Mn_3O_4-CNTs show that the characteristic diffraction peaks remain largely consistent with those of the pristine sample, indicating that the crystal structure is preserved. TEM imaging further confirms that the cubic morphology of Mn_3O_4 within FePc-Mn_3O_4-CNTs is maintained after 10,000 cycles. In addition, XPS analysis reveals that the binding energies and peak areas of Fe 2p, Mn 2p, and N 1s remain essentially unchanged after 10,000 cycles, demonstrating that the chemical valence states of Fe and Mn are stable. In summary, post-reaction XRD, TEM, and XPS analysis of FePc-Mn_3O_4-CNTs and FePc-CNTs reveals that their crystal structures and chemical states remain largely unchanged (Figs. S24–S26 in the ESM). These integrated results demonstrate that the engineered Fe-O linkage within the asymmetric Fe-N_4-O configuration is pivotal: It optimizes the electronic structure of the iron center for enhanced intrinsic activity and kinetics, reinforces the interface with the Mn_3O_4-CNTs support, and leads to improved charge transfer, expanded active area, and exceptional structural stability during ORR.

To deeply investigate the synergistic mechanism between axial coordination and the heterojunction interface and its enhancement effect on the ORR performance of FePc-Mn_3O_4, density functional theory (DFT) calculations were further performed. Based on experimental characterizations (HAADF-STEM and EXAFS), a simplified theoretical model featuring an axial Fe-O coordination interface was constructed, as presented in Fig. 4(a).

Charge density difference analysis (Fig. 4(a)) shows axial charge accumulation between Fe and the axially coordinated O atom, accompanied by significant charge depletion around the Fe center, confirming electron transfer from the Fe site to the axial O atom and resulting in a pronounced redistribution of electron density perpendicular to the FePc plane. Bader charge analysis further indicates that the Fe-N_4 center in FePc-Mn_3O_4 loses additional electrons through the axial Fe-O coordination heterojunction built-in electric field (BIEF) effect, with the electron count at the Fe center decreasing from 6.87e to 6.67e (a reduction of 0.2e), and approximately 1.25e transferred from FePc to Mn_3O_4, thereby forming an electron-deficient Fe-N_4 active center [44].

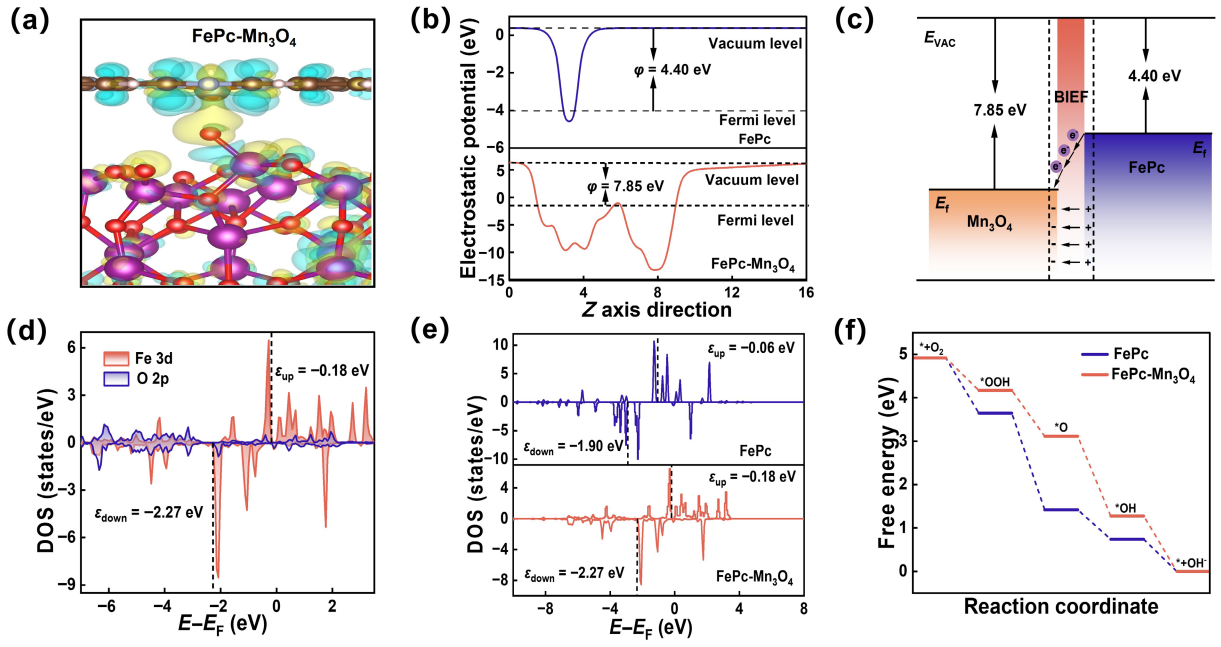

Figure 4 (a) Charge density difference of FePc-Mn_3O_4.Yellow and cyan isosurfaces represent electron accumulation and depletion, respectively. (b) Calculated work functions of FePc and Mn_3O_4. (c) Schematic illustration of the built-in electric field between FePc and Mn_3O_4. (d) PDOS of FePc-Mn_3O_4. (e) PDOS plots of the Fe 3*d* orbitals in FePc and FePc-Mn_3O_4, along with the corresponding *d*-band centers. (f) Free-energy diagrams of the ORR intermediates on FePc-Mn_3O_4.

Work function calculations (Figs. 4(b) and 4(c)) show that the work function of FePc is 4.40 eV, while that of Mn_3O_4 is 7.85 eV. The higher Fermi level of FePc relative to Mn_3O_4 drives electron flow from FePc to Mn_3O_4, consistent with the charge depletion at the Fe center observed in the charge density difference analysis. This interfacial electron transfer spatially separates positive and negative charges, inducing charge polarization at the interface. Thus, under the BIEF effect at the axial Fe-O coordination interface, FePc exhibits pronounced charge polarization on Mn_3O_4, in agreement with the XPS and XANES analyses.

To explore the regulatory mechanism of axial coordination on the electronic structure, density of states (DOS) analysis was performed. The projected density of states (PDOS) results (Fig. 4(d)) show partial overlap between the PDOS of Fe and O in FePc-Mn_3O_4, indicating strong interaction between the Fe site and the axial O atom. The total DOS analysis (Fig. S27(a) in the ESM) reveals that the electronic density of states at the Fermi level is significantly higher for FePc-Mn_3O_4 than for FePc, suggesting superior electrical conductivity and charge transport capability.

Furthermore, PDOS analysis (Fig. 4(e)) demonstrates the modulation of the Fe d-band center by the BIEF effect at the axial heterojunction interface. In FePc-Mn_3O_4, the *d*-band center of Fe shifts downward significantly. Specifically, the spin-up peak shifts from –0.06 to –0.18 eV, and the spin-down peak shifts from –1.90 to –2.27 eV, lowering the average *d*-band center from –0.98 to –1.225 eV. Together with the charge loss at the Fe center revealed by Bader charge analysis, this indicates that axial coordination weakens the adsorption strength between Fe and oxygen-containing intermediates.

The ORR free energy diagram of FePc-Mn_3O_4 (Fig. 4(f)) shows that at U = 0 V, the free energy changes for each reaction step (ΔG_1 to ΔG_4) are more uniform compared to those of FePc (Fig. S27(b) in the ESM), indicating that the energy barriers for each step are more balanced, thereby effectively reducing the overpotential for ORR [47]. Additionally, in the FePc-Mn_3O_4 heterojunction, the rate-determining step shifts from *OOH → *O to *O → *OH, suggesting that the synergistic effect of axial Fe-O coordination and the interfacial built-in electric field enhances ORR by facilitating O-O bond cleavage in *OOH [46, 48]. This synergy modulates the electronic structure of the Fe active center, shifting the *d*-band center downward and enabling balanced adsorption and desorption of oxygen intermediates.

To evaluate the FePc-Mn_3O_4-CNTs catalyst in a practical zinc-air battery system, a custom battery was assembled using a zinc-foil anode paired with a FePc-Mn_3O_4-CNTs/RuO_2 composite cathode (Fig. 5(a)). The assembled battery delivered an open-circuit potential (OCP) of 1.50 V, approximately 140 mV higher than the 20% Pt/C-RuO_2 reference (~1.36 V) and closer to the theoretical value of 1.65 V (Fig. 5(b), Fig. S28(a) in the ESM). Comparative electrochemical analysis shows that the FePc-Mn_3O_4-CNTs/RuO_2 battery achieves a higher discharge current density with a smaller voltage gap during cycling (Fig. S28(b) in the ESM). The battery reaches a peak power density of 171.81 mW·cm^{-2}, about 1.53 times higher than the 112.07 mW·cm^{-2} of the 20% Pt/C-RuO_2 benchmark (Fig. 5(c)). It also exhibits a specific capacity of 754.12 mAh·g_{Zn}^{-1} at 5 mA·cm^{-2}, outperforming the reference (709.50 mAh·g_{Zn}^{-1}) by ~6.3% (Fig. 5(e)). Step-wise current tests between 2 and 10 mA·cm^{-2} show stable discharge voltages without noticeable decay, with rapid recovery to the initial value when the current density is reset to 2 mA·cm^{-2}, reflecting the catalyst's high structural integrity and excellent reaction reversibility Rechargeable batteries subjected to extended cycling at 10 mA·cm^{-2} (0.5 h each for discharge and charge) demonstrate outstanding stability over 160 h without significant voltage-gap widening (Fig. 5(g)), nearly eight times longer than the 20 h sustained by the 20% Pt/C-RuO_2 counterpart. These results underscore the operational advantages of the FePc-Mn_3O_4-CNTs/RuO_2 catalyst in zinc-air batteries and affirm its potential for integration into practical energy-storage solutions (Fig. 5(d)).

4 Conclusions

In summary, an oxygen-bridged axial coordination strategy was used to synthesize a FePc-Mn_3O_4-CNTs catalyst with an

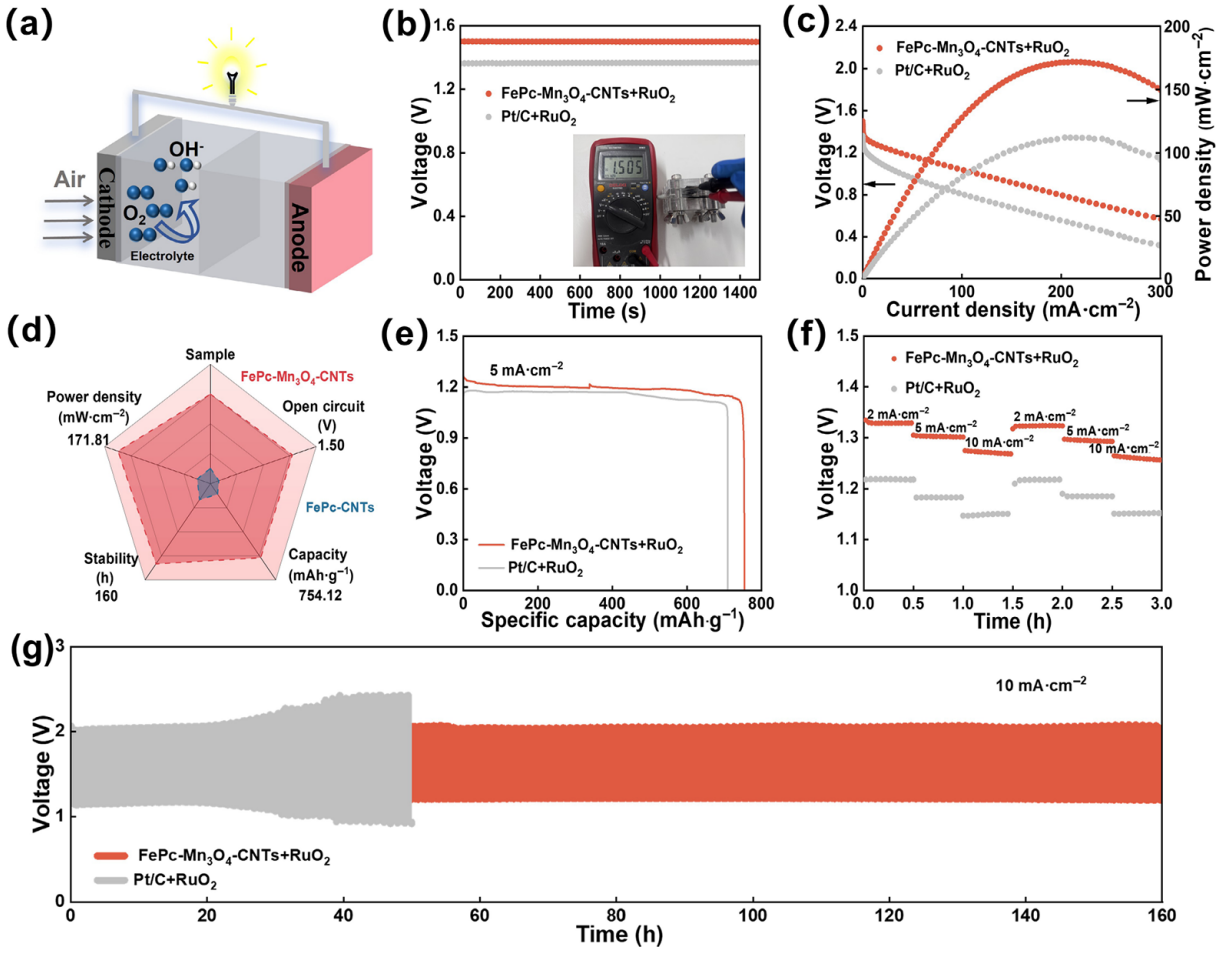

Figure 5 (a) Schematic of the constructed zinc air battery. (b) Open-circuit voltage (OCP) profiles. (c) Polarization and corresponding power density curves. (d) Summary of key performance parameters. (e) Galvanostatic discharge curves at 5 mA·cm^{-2}. (f) Rate capability tests at different current densities. (g) Long-term galvanostatic charge-discharge cycling curves at 10 mA·cm^{-2}.

asymmetric Fe-N_4-O coordination architecture. This design enables synergistic adjustment of the Fe-site coordination geometry through axial bonding while improving charge transport via heterojunction interface effects. XAS analysis confirms that the FePc moiety undergoes a symmetry transition from D_{4h} to C_{4v}, forming an asymmetric Fe-N_4-O coordination structure. DFT calculations further demonstrate that this axial Fe-O coordination heterojunction BIEF effect induces electron transfer from the Fe center to the axial O atom and downshifts the Fe *d*-band center, thereby weakening the adsorption of oxygen-containing intermediates and achieving a balanced adsorption-desorption state. The synergy between axial coordination and heterointerface engineering markedly boosts ORR catalytic performance, yielding a half-wave potential of 0.89 V vs. RHE. In a zinc-air battery, FePc-Mn_3O_4-CNTs delivers a high power density (171.81 mW·cm^{-2}) and stable operation exceeding 160 h, demonstrating strong practical potential. Despite these promising results in alkaline media, the catalyst's performance and stability in acidic media remain to be optimized in future work. Moreover, further efforts should be directed toward simplifying the synthesis process to evaluate its feasibility for large-scale production, thereby facilitating the practical deployment of this molecular design strategy. This work introduces a synergistic approach combining axial coordination engineering and heterojunction design, advancing the development of efficient Fe-N-C molecular catalysts for zinc-air batteries.

Acknowledgements

This work was supported by National Natural Science Foundation of China (22572035, 22472023); The Fundamental Research Funds for the Central Universities (2412024QD014 and 2412023QD019), Science and Technology Program of the Ministry of Public Security of China (2025JSM11), and the Jilin Province Science and Technology Development Program (20250102077JC).

Declaration of conflicting interests

The authors declare no conflicting interests regarding the content of this article.

Data availability

All data needed to support the conclusions in the paper are presented in the manuscript and/or the Supplementary Materials. Additional data related to this paper may be requested from the corresponding author upon request.

Author contributions

Z. H. X. and J. F. C. led the project. W. L. performed the experiments. J. X. assisted with the sample synthesis. Y. L. contributed to TEM characterizations. M. T. H. helped with the

zinc-air battery tests. N. M. and X. W. G. helped with ORR performance measurements. M.Y.W. helped conducted the XAS tests. All authors discussed the results and provided comments. All authors have approved the final version of the manuscript.

Electronic Supplementary Material: Supplementary material (characterization, electrochemical measurements, assembly of Zn-air battery, figures of SEM, TEM, UPS, Raman, XPS, EXAFS, and ORR tests of as-prepared samples, as well as tables of ORR performance) is available in the online version of this article at https://doi.org/10.26599/NRE.2026.9120232.

References

[1] Yu, A.; Yang, Y. Atomically dispersed metal catalysts for oxygen reduction reaction: Two-electron vs. four-electron pathways. *Angew. Chem., Int. Ed.* **2025**, *64*, e202424161.

[2] Huo, M. T.; Liang, Y.; Liu, W.; Zhang, X. Y.; Qin, K. C.; Ma, Y.; Xing, Z. H.; Chang, J. F.; Zhu, G. S. Synergistically promoting oxygen electrocatalysis through the precise integration of atomically-dispersed Fe sites and Co nanoparticles. *Adv. Energy Mater.* **2026**, *16*, 2405155.

[3] Jiao, K.; Xuan, J.; Du, Q.; Bao, Z. M.; Xie, B.; Wang, B. W.; Zhao, Y.; Fan, L. H.; Wang, H. Z.; Hou, Z. J. et al. Designing the next generation of proton-exchange membrane fuel cells. *Nature* **2021**, *595*, 361–369.

[4] Yi, S. Y.; Choi, E.; Jang, H. Y.; Lee, S.; Park, J.; Choi, D.; Jang, Y.; Kang, H.; Back, S.; Jang, S. et al. Insight into defect engineering of atomically dispersed iron electrocatalysts for high-performance proton exchange membrane fuel cell. *Adv. Mater.* **2023**, *35*, 2302666.

[5] Zhang, W.; Chang, J. F.; Yang, Y. Strong precious metal-metal oxide interaction for oxygen reduction reaction: A strategy for efficient catalyst design. *SusMat* **2023**, *3*, 2–20.

[6] Liu, M. N.; Liu, Y. X.; Zhang, X.; Li, L. F.; Xue, X. Y.; Humayun, M.; Yang, H. W.; Sun, L. B.; Bououdina, M.; Zeng, J. R. et al. Altering the symmetry of Fe–N–C by axial Cl-mediation for high-performance zinc-air batteries. *Angew. Chem., Int. Ed.* **2025**, *64*, e202504923.

[7] Cheng, Y. J.; Wang, H.; Song, H. Q.; Zhang, K.; Waterhouse, G. I. N.; Chang, J. W.; Tang, Z. Y.; Lu, S. Y. Design strategies towards transition metal single atom catalysts for the oxygen reduction reaction-a review. *Nano Res. Energy* **2023**, *2*, e9120082.

[8] Debe, M. K. Electrocatalyst approaches and challenges for automotive fuel cells. *Nature* **2012**, *486*, 43–51.

[9] Zhang, H. W.; Chen, H. C.; Feizpoor, S.; Li, L. F.; Zhang, X.; Xu, X. F.; Zhuang, Z. C.; Li, Z. S.; Hu, W. Y.; Snyders, R. et al. Tailoring oxygen reduction reaction kinetics of Fe–N–C catalyst via spin manipulation for efficient zinc-air batteries. *Adv. Mater.* **2024**, *36*, 2400523.

[10] Guo, F. J.; Zhang, M. Y.; Yi, S. C.; Li, X. X.; Xin, R.; Yang, M.; Liu, B.; Chen, H. B.; Li, H. M.; Liu, Y. J. Metal-coordinated porous polydopamine nanospheres derived Fe_3N–FeCo encapsulated N-doped carbon as a highly efficient electrocatalyst for oxygen reduction reaction. *Nano Res. Energy* **2022**, *1*, e9120027.

[11] Salah, A.; Ren, H. D.; Al-Ansi, N.; Tan, H. Q.; Yu, F. Y.; Yanchun, L.; Thamer, B. M.; Al-Salihy, A.; Zhao, L.; Li, Y. G. Dispersing small Ru nanoparticles into boron nitride remodified by reduced graphene oxide for high-efficient electrocatalytic hydrogen evolution reaction. *J. Colloid Interface Sci.* **2023**, *644*, 378–387.

[12] Liu, W.; Liang, Y.; Huo, M. T.; Ma, N.; Qin, K. C.; Chang, J. F.; Xing, Z. H. Ligand engineering of Co-MOF-74 with hexaaminotriphenylene for enhanced oxygen reduction reaction in zinc-air batteries. *Nano Res.* **2025**, *18*, 94907195.

[13] Sui, R.; Liu, B.; Chen, C.; Tan, X.; He, C.; Xin, D. Y.; Chen, B. W.; Xu, Z. Y.; Li, J. Z.; Chen, W. X. et al. Constructing asymmetric Fe–Nb diatomic sites to enhance ORR activity and durability. *J. Am. Chem. Soc.* **2024**, *146*, 26442–26453.

[14] Zeng, Y. C.; Li, C. Z.; Li, B. Y.; Liang, J. S.; Zachman, M. J.; Cullen, D. A.; Hermann, R. P.; Alp, E. E.; Lavina, B.; Karakalos, S. et al. Tuning the thermal activation atmosphere breaks the activity-stability trade-off of Fe–N–C oxygen reduction fuel cell catalysts. *Nat. Catal.* **2023**, *6*, 1215–1227.

[15] Liu, J. B.; Liu, Y.; Nan, B.; Wang, D. S.; Allen, C.; Gong, Z. C.; He, G. C.; Fu, K. X.; Ye, G. L.; Fei, H. L. A two-in-one strategy to simultaneously boost the site density and turnover frequency of Fe–N–C oxygen reduction catalysts. *Angew. Chem., Int. Ed.* **2025**, *64*, e202425196.

[16] Song, W. Q.; Xiao, C. X.; Ding, J.; Huang, Z. C.; Yang, X. Y.; Zhang, T.; Mitlin, D.; Hu, W. B. Review of carbon support coordination environments for single metal atom electrocatalysts (SACs). *Adv. Mater.* **2024**, *36*, 2301477.

[17] Li, Z. W.; Xie, Y.; Han, Y. K.; Wang, H. Z.; Gao, J. X.; Chen, L.; Xu, L.; Lu, L. G.; Zhao, Y.; Wang, E. D. et al. Unraveling the significance of FeN_4 and Fe_3S_4 active species for sustained direct ammonia fuel cells and zinc-air batteries. *Nano Res. Energy* **2025**, *4*, e9120169.

[18] Zhao, K. M.; Wu, D. X.; Wu, W. K.; Nie, J. B.; Geng, F. S.; Li, G.; Shi, H. Y.; Huang, S. C.; Huang, H.; Zhang, J. et al. Identifying high-spin hydroxyl-coordinated $Fe^{3+}N_4$ as the active centre for acidic oxygen reduction using molecular model catalysts. *Nat. Catal.* **2025**, *8*, 422–435.

[19] Li, L. B.; Tang, X. N.; Huang, S. H.; Lu, C. B.; Lützenkirchen-Hecht, D.; Yuan, K.; Zhuang, X. D.; Chen, Y. W. Longitudinally grafting of graphene with iron phthalocyanine-based porous organic polymer to boost oxygen electroreduction. *Angew. Chem., Int. Ed.* **2023**, *62*, e202301642.

[20] Xie, P. F.; Zhong, H.; Fang, L. Z.; Lyu, Z.; Yu, W. J.; Li, T.; Lee, J.; Shin, H.; Beckman, S. P.; Lin, Y. H. et al. Molecular Fe–N_4 moieties coupled with atomic Co–N_4 sites toward improved oxygen reduction performance. *Adv. Funct. Mater.* **2024**, *34*, 2314554.

[21] Ding, S. C.; He, L.; Fang, L. Z.; Zhu, Y. Z.; Li, T.; Lyu, Z.; Du, D.; Lin, Y. H.; Li, J. C. Carbon-nanotube-bridging strategy for integrating single Fe atoms and NiCo nanoparticles in a bifunctional oxygen electrocatalyst toward high-efficiency and long-life rechargeable zinc-air batteries. *Adv. Energy Mater.* **2022**, *12*, 2202984.

[22] Hu, H.; Meng, Y.; Mei, Y.; Hou, P. X.; Liu, C.; Cheng, H. M.; Shao, M. H.; Li, J. C. Bifunctional oxygen electrocatalysts enriched with single Fe atoms and $NiFe_2O_4$ nanoparticles for rechargeable zinc-air batteries. *Energy Storage Mater.* **2023**, *54*, 517–523.

[23] Win, P. E. P.; Yang, J. H.; Ning, S. W.; Huang, X.; Fu, G. T.; Sun, Q. M.; Xia, X. H.; Wang, J. Molecular architectures of iron complexes for oxygen reduction catalysis-activity enhancement by hydroxide ions coupling. *Proc. Natl. Acad. Sci. USA* **2024**, *121*, e2316553121.

[24] Qin, Y.; Chuang, C. H.; Liu, X. J.; Liang, X.; Xie, L. F.; Wang, K.; Pao, C. W.; Lu, Y. R.; Liu, Y.; Chen, Y. W. et al. DNA-anchored single-molecule iron phthalocyanine as an efficient electrocatalyst for alkaline fuel cells. *ACS Catal.* **2024**, *14*, 7514–7525.

[25] Musgrave, C. B.; Su, J. J.; Xiong, P.; Song, Y.; Huang, L. B.; Liu, Y.; Li, G.; Zhang, Q.; Xin, Y. E.; Li, M. M. J. et al. Molecular strain accelerates electron transfer for enhanced oxygen reduction. *J. Am. Chem. Soc.* **2025**, *147*, 3786–3795.

[26] Li, L. F.; Liu, Y. X.; Zhang, X.; Humayun, M.; Yang, H. W.; Zeng, J. R.; Younus, H. A.; Pang, Y. J.; Wang, D. L.; Snyders, R. et al. Curvature strain-induced electron spin leveraging in d orbitals toward oxygen reduction for Zn-air batteries. *Nano Lett.* **2025**, *25*, 16459–16467.

[27] Chen, K. J.; Liu, K.; An, P. D.; Li, H. J. W.; Lin, Y. Y.; Hu, J. H.; Jia, C. K.; Fu, J. W.; Li, H. M.; Liu, H. et al. Iron phthalocyanine with coordination induced electronic localization to boost oxygen reduction reaction. *Nat. Commun.* **2020**, *11*, 4173.

[28] Fan, W. J.; Duan, Z. Y.; Liu, W.; Mehmood, R.; Qu, J. T.; Cao, Y. C.; Guo, X. Y.; Zhong, J.; Zhang, F. X. Rational design of heterogenized molecular phthalocyanine hybrid single-atom electrocatalyst towards two-electron oxygen reduction. *Nat.*

Commun. **2023**, *14*, 1426.
[29] Yan, Z. J.; Cui, B.; Li, N.; Yang, D. Q.; Xie, J. L.; Geng, T. F.; Qiao, Y. M.; Jiang, Y.; Bu, N. S.; Yuan, Y. et al. Dimensionality control of 1D coupling reaction for the facile preparation of porous carbon nanofibers. *Inorg. Chem.* **2021**, *60*, 18058–18064.
[30] Dai, Y. K.; Liu, B.; Zhang, Z. Y.; Guo, P.; Liu, C.; Zhang, Y. L.; Zhao, L.; Wang, Z. B. Tailoring the d-orbital splitting manner of single atomic sites for enhanced oxygen reduction. *Adv. Mater.* **2023**, *35*, 2210757.
[31] Su, X. R.; Hu, B. T.; Zhang, Y. Z.; Liu, C. H.; Wang, C. Y.; Zheng, L. R.; Zhao, D.; Zhang, J. T.; Chen, C. Built-in axial electric field-driven electron-rich monomolecular Co sites for promoting CO_2 electroreduction to CO over ultrawide potential window. *Angew. Chem., Int. Ed.* **2025**, *64*, e202511671.
[32] Yu, Y.; Shi, J. L.; Li, M. H.; Li, L. R.; Hu, J. S.; Li, S. F.; Zhang, J. N. Local magnetic effect-induced electron configuration regulation: Spin flipping of iron centers for molecular catalysis. *ACS Catal.* **2024**, *14*, 7191–7200.
[33] Li, T.; Tong, J. J.; Liu, S. Y.; Liang, J. Y.; Dai, G. L.; Sun, W. T.; Sun, A. K. Butterfly-tie like $MnCO_3$@Mn_3O_4 heterostructure enhanced the electrochemical performances of aqueous zinc ion batteries. *J. Colloid Interface Sci.* **2024**, *656*, 504–512.
[34] Mei, Z. Y.; Cai, S.; Zhao, G. F.; Zou, X. X.; Fu, Y.; Jiang, J. W.; An, Q.; Li, M.; Liu, T. T.; Guo, H. Boosting the ORR active and Zn-air battery performance through ameliorating the coordination environment of iron phthalocyanine. *Chem. Eng. J.* **2022**, *430*, 132691.
[35] Gan, M. L.; Lu, C. J.; Feng, W. H.; He, C.; Hu, J. P.; Xie, F. X.; He, W.; Sun, Z. M. Rational design of efficient Zn–CoNi/air hybrid batteries via charge redistribution in iron phthalocyanine modified cobalt-nickel layered double hydroxide. *Energy Storage Mater.* **2026**, *84*, 104755.
[36] Meng, L. Z.; Niu, S. W.; Wei, Z. Y.; Qin, X.; Naseem, F.; Wei, W. Accelerated proton-coupled electron transfer kinetics of iron phthalocyanine for oxygen reduction via heteropoly blue clusters. *Appl. Catal. B: Environ. Energy* **2025**, *367*, 125080.
[37] Chen, J.; Chu, K.; Sun, S. Q.; Chen, H.; Song, B. H.; Wang, J. H.; Liu, Z. D.; Zhu, L. Synthesis of magnetic core-shell Fe_3O_4–Mn_3O_4 composite for degradation of sulfadiazine via peroxymonosulfate activation: Characterization, mechanism and toxicity analysis. *J. Environ. Chem. Eng.* **2023**, *11*, 109230.
[38] Jiang, Y. M.; Song, Z. K.; Qu, M. J.; Jiang, Y.; Luo, W.; He, R. X. Co–Mn bimetallic nanowires by interfacial modulation with/without vacancy filling as active and durable electrocatalysts for water splitting. *Small* **2024**, *20*, 2400859.
[39] Nie, Z. F.; Zhang, L. L.; Ding, X.; Cong, M. Y.; Xu, F. F.; Ma, L. H.; Guo, M. X.; Li, M. Z.; Zhang, L. X. Catalytic kinetics regulation for enhanced electrochemical nitrogen oxidation by Ru-nanoclusters-coupled Mn_3O_4 catalysts decorated with atomically dispersed Ru atoms. *Adv. Mater.* **2022**, *34*, 2108180.
[40] Wu, Y.; Chen, J. L.; Liu, J.; Zhang, L. J.; Abazari, R.; Li, T. T.; Qian, J. J. Iron phthalocyanine coupled with Co–N_x sites in carbon nanostraws for Zn-air batteries. *Chem. Eng. J.* **2025**, *503*, 158343.
[41] Zhang, H.; Zhang, Z. K.; Zhang, Z.; Li, Y. F.; Hou, Y.; Liu, P. Z.; Xu, B. S.; Zhang, H. X.; Liu, Y. Z.; Guo, J. J. Highly dispersed ultrasmall iron phthalocyanine molecule clusters confined by mesopore-rich N-doped hollow carbon nanospheres for efficient oxygen reduction reaction and Zn-air battery. *Chem. Eng. J.* **2023**, *469*, 143996.
[42] Su, J. J.; Musgrave, C. B.; Song, Y.; Huang, L. B.; Liu, Y.; Li, G.; Xin, Y. E.; Xiong, P.; Li, M. M. J.; Wu, H. R. et al. Strain enhances the activity of molecular electrocatalysts via carbon nanotube supports. *Nat. Catal.* **2023**, *6*, 818–828.
[43] Xiang, R. N.; Kang, J. W.; Zhang, L.; Qin, X. P.; Liao, P. S.; Zhan, S. J.; Liu, Q. H.; Liu, Z.; Gao, S.; Li, G. Q. Ni-mediated high-spin iron(III) for boosting electrocatalytic NO to oxime conversion. *Angew. Chem., Int. Ed.* **2025**, *64*, e202515660.
[44] Guo, X. L.; Sun, H.; Li, C. G.; Zhang, S. Q.; Li, Z. H.; Hou, X. Y.; Chen, X. B.; Liu, J. Y.; Shi, Z.; Feng, S. H. Defect-engineered Mn_3O_4/CNTs composites enhancing reaction kinetics for zinc-ions storage performance. *J. Energy Chem.* **2022**, *68*, 538–547.
[45] Zhao, M. M.; Wang, Y. J.; Jiang, Z. Q.; Zhu, J. Q.; Jiang, Z. J. Built-in-electric field and carbon nanotube supporting enabled Co_3O_4/CeO_2heterostructures with efficient and durable activities for nitrate-to-ammonia conversion. *Appl. Catal. B: Environ. Energy* **2026**, *384*, 126186.
[46] Cheng, R. Q.; He, X. Q.; Jiang, M.; Shao, X. C.; Tang, W. Q.; Ran, B.; Li, H. X.; Fu, C. P. f-p-d gradient orbital coupling induced spin state enhancement of atomic Fe sites for efficient and stable oxygen reduction reaction. *Adv. Funct. Mater.* **2025**, *35*, 2425138.
[47] Li, K. Q.; Wang, C. Q.; Li, H. X.; Wen, Y. L.; Wang, F.; Xue, Q. Y.; Huang, Z. Y.; Fu, C. P. Heterostructural interface in Fe_3C–TiN quantum dots boosts oxygen reduction reaction for Al-air batteries. *ACS Appl. Mater. Interfaces* **2021**, *13*, 47440–47448.
[48] Hu, X.; Chen, S. Y.; Chen, L. T.; Tian, Y.; Yao, S.; Lu, Z. Y.; Zhang, X.; Zhou, Z. What is the real origin of the activity of Fe–N–C electrocatalysts in the O_2 reduction reaction? Critical roles of coordinating pyrrolic N and axially adsorbing species. *J. Am. Chem. Soc.* **2022**, *144*, 18144–18152.

Wei Liu is currently a Ph.D. candidate under the supervision of Prof. Chang at the Faculty of Chemistry, Northeast Normal University. Her research focuses on the design and controllable synthesis of low-precious or non-precious metal electrocatalysts.

Zihao Xing is an Associate Professor and Doctoral Supervisor at the Faculty of Chemistry, Northeast Normal University. He completed his B.S., M.S., and Ph.D. consecutively at the College of Chemistry, Jilin University. His research primarily focuses on the design and controllable synthesis of low-precious or non-precious metal electrocatalysts for applications in fuel cells, metal-air batteries, and water splitting. He has published over 40 papers in leading journals, including *Journal of the American Chemical Society*, *Angewandte Chemie International Edition*, *Advanced Materials*, and *Advanced Energy Materials*. Additionally, he serves as a Young Editorial Board Member for several journals, including *Nano Research Energy* and *eScience*.

Jinfa Chang is a Professor and Doctoral Supervisor at the Faculty of Chemistry, Northeast Normal University. His research focuses on surface and interface electrochemistry of energy materials and devices, materials science, electrochemical engineering, and nanoscience technology. He has published more than 70 SCI-indexed papers on high-impact journals-including *Nature Energy*, *Nature Communications*, *Journal of the American Chemical Society*, *Angewandte Chemie International Edition*, *Advanced Materials*, *Energy & Environmental Science*, and *Joule*, accumulating over 5400 citations on Google Scholar and achieving an H-index of 41. He also holds editorial roles as an Editorial Board Member of *Spotlight Reporters of Chinese Journal of Chemistry*, a Young Editorial Board Member of *eScience*, *Nano Research*, and *Nano Research Energy*.